Shock-wave/turbulent boundary-layer interaction over a flexible panel

Laguarda, L.; Hickel, S.; Schrijer, F.F.J.; van Oudheusden, B.W.

Important note
To cite this publication, please use the final published version (if applicable).
Please check the document version above.

Shock-wave/turbulent boundary-layer interaction over a flexible panel

L. Laguarda, S. Hickel, F. F. J. Schrijer and B. W. van Oudheusden

Aerodynamics Group, Department of Flow Physics and Technology, Faculty of Aerospace Engineering, Delft University of Technology, Delft, The Netherlands, 2629HS

Wall-resolved large-eddy simulations (LES) are carried out to investigate the aeroelastic coupling between a Mach 2.0 **impinging shock-wave/turbulent boundary-layer interaction (STBLI) and a flexible thin-panel. After the initial transient, the panel exhibits self-sustained oscillatory behavior with varying oscillation amplitude, confirming the strong and complex dynamic coupling over a broad frequency range. The first three bending modes of the panel oscillation are found to contribute most to the unsteady panel response. The observed modal frequencies are in close agreement with natural frequencies of the pre-stressed panel, which differ significantly from the natural frequencies of the unloaded flat panel. This highlights the importance of the mean panel deformation and the corresponding stiffening in the fluid-structure interaction (FSI) dynamics. Mean-flow shows an enlarged reverse-flow region compared to a flat rigid-wall STBLI at the same flow conditions. The separation shock is also located further upstream in the coupled case, and wall-pressure fluctuations have a higher peak at the separation-shock foot. Spectral analysis of wall-pressure, separation-shock location and bubble-volume signals indicates that the STBLI flow resonates with the panel oscillation, primarily at the first bending frequency. This is further confirmed by sparsity-promoting dynamic mode decomposition of the flow and displacement data, which identifies this frequency as the most dominant and successfully isolates the associated FSI dynamics. Based on present results, it is clear that dynamic FSI involving STBLI and flexible panels accentuates the undesirable features of STBLI.**

I. Introduction

A central concern in the structural design of high-speed systems is the exposure to shock-wave/turbulent boundary-layer interactions (STBLIs). These complex multi-scale flow phenomena exhibit energetic low-frequency motions that impose intermittent and high-amplitude pressure loads on nearby components [1–3]. Lightweight skin panels may resonate under these conditions, which can lead to vibrational fatigue [4]. At very high speeds, STBLIs additionally lead to severe localized heating [5], which can further degrade the mechanical properties of aircraft components [6]. The accurate characterization of dynamic fluid-structure interactions (FSIs) is therefore paramount for the design of high-speed flight vehicles with expanded operational envelopes [7].

Most prior work on STBLI has been performed on rigid geometries, often of canonical type like flat plates, compression ramps and steps [8]. The wide range of Mach number, Reynolds number and shock strength covered through experimentation, and more recently, with high-fidelity numerical simulations, has helped shape our fundamental understanding of the relevant flow physics [9]. The interaction between STBLI and elastic components, on the other hand, has been far less studied than the baseline case with rigid walls [10]. The presence of a compliant structure brings a new dimension of complexity to the STBLI flow that may substantially alter its characteristic unsteadiness [11]. Recent studies involving STBLI and flexible panels, which are predominantly of experimental nature, suggest that this is the case [12, 13] and that the flow efficiently triggers low-order modes of panel vibration [14–16]. However, questions still remain regarding the coupling mechanism and the particular role of static and dynamic surface displacements in the modulation of STBLI, and these questions need to be addressed in order to efficiently mitigate the impact of STBLI on structural components.

In this study, we thus perform wall-resolved large-eddy simulations (LES) of a Mach 2.0 impinging STBLI over a flexible thin-panel to investigate the resulting dynamic coupling. A partitioned FSI approach is employed for the calculations, comprising a finite-volume fluid solver and a finite-element structural solver combined with the adaptive reduced-order model (AROM) of Thari et al. [17]. To capture the full-range of low-frequency dynamics, the simulation is integrated for more than 90 flow-through times of the full domain length after the initial transient. A strong and self-sustained dynamic coupling is observed between the flow and the structure, which is accurately characterized.
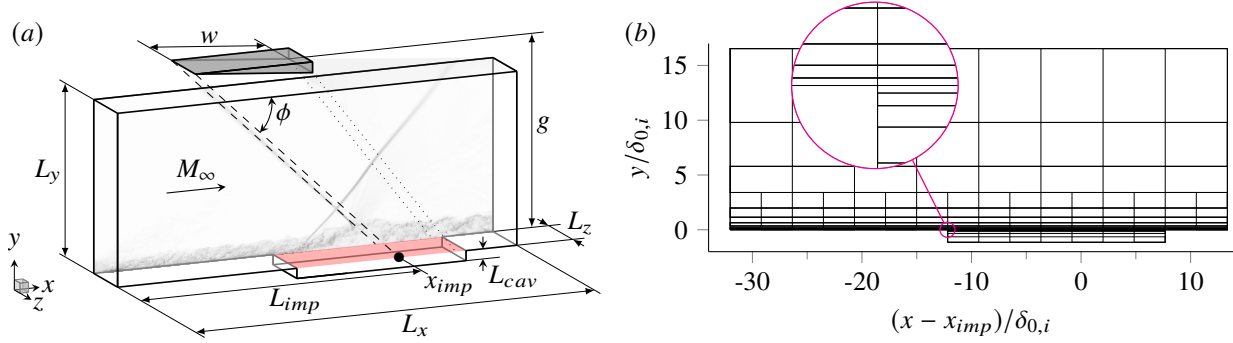
Fig. 1   (a) Schematics of the computational domain, and (b) block distribution of the computational grid.

Results are compared against a flat rigid-wall STBLI at the same flow conditions.

II. Problem formulation

The investigated flow geometry is outlined in figure 1(a). It involves an oblique shock wave impinging a turbulent boundary layer (TBL) over a compliant panel (the latter shown in red). The free-stream flow is air at Mach number $M_\infty = 2.0$ and has a stagnation temperature and pressure of $T_0 = 288$ K and $p_0 = 356$ kPa, respectively. The 99% velocity-based boundary layer thickness at the inflow plane $\delta_{0,i}$ is 5.2 mm, and the corresponding Reynolds number based on free-stream quantities is $Re_{\delta_{0,i}} = \rho_\infty u_\infty \delta_{0,i}/\mu_\infty = 50.1 \times 10^3$. The panel has a thickness $h = 0.25$ mm and consists of Aluminium 7075-T6 with a Young's modulus of $E = 71.1$ GPa, a Poisson ratio of $\nu = 0.33$ and a density of $\rho_S = 2800$ kg m^{-3}. The length of the panel is $a = 100$ mm and the panel is clamped at front and rear with free side edges. The corresponding non-dimensional dynamic pressure parameter, commonly used in standard panel flutter studies, is $\lambda = \rho_\infty u_\infty^2 a^3 D^{-1} = 2440$, where $D = Eh^3/(12(1 - \nu^2))$ is the flexural rigidity of the panel. The flow deflection induced by the virtual shock generator is $\vartheta = 10.66°$ which results in an oblique shock wave with wave angle $\phi = 40.04°$ and pressure ratio $\Pi = 1.76$. The shock generator is placed at a height $g = 96$ mm above the surface, while its streamwise position is set such that the theoretical inviscid shock impingement point x_{imp} occurs at 60% of the panel length and is located $L_{imp} = 32\delta_{0,i}$ downstream of the inflow plane. The considered channel height to wedge hypotenuse ratio is $g/w = 1.16$, see figure 1(a).

III. Numerical approach

The fluid domain is solved with the finite-volume solver INCA (https://www.inca-cfd.com), which employs the adaptive local deconvolution method (ALDM) for implicit LES of the compressible Navier-Stokes equations [18]. ALDM is a nonlinear solution-adaptive finite volume method that exploits the discretization of the convective fluxes to introduce a physically consistent sub-grid scale turbulence model. Since unresolved turbulence and shock waves require fundamentally different modeling, ALDM relies on a shock sensor to control model parameters. This guarantees the accurate propagation of smooth waves and turbulence without excessive numerical dissipation while providing essentially non-oscillatory solutions at strong discontinuities. Diffusive fluxes are approximated by linear second-order schemes and a third-order total variation diminishing Runge–Kutta scheme is employed for time integration. The reader is referred to Hickel et al. [18] for implementation details of the method and validation results.

The computational domain is rectangular with dimensions $[L_x, L_y, L_z] = [45, 16.5, 4]\delta_{0,i}$, see figure 1(a). The inflow plane is located at $(x - x_{imp}) = -32\delta_{0,i}$ and $(x - x_{imp}) = -11.6\delta_{0,i}$ is the leading edge of the panel. Non-reflecting boundary conditions are used at the top and outflow boundaries, and periodicity is imposed in the spanwise direction. The wall is modeled as isothermal at the free-stream stagnation temperature, and the incident shock and trailing-edge expansion fan are introduced at the top boundary via the Rankine-Hugoniot relations and Prandtl-Meyer theory, respectively. At the inflow plane, turbulent boundary conditions with well-defined space and time correlations are prescribed via the digital filter technique of Xie & Castro [19]. The target mean and fluctuating velocity profiles are derived from the DNS data of Pirozzoli and Bernardini [20] at $Re_\tau = 900$, and the reader is referred to Laguarda

2

and Hickel [21] for details on the filtering procedure (the employed settings correspond to those for case $A2$ in their publication). Furthermore, the cut-cell immersed boundary method (IBM) of Pasquariello et al. [22] is employed to accurately represent the moving panel on the Cartesian grid. A small cavity is therefore added underneath the panel ($L_{cav} = \delta_{0,i}$) to allow for negative displacements of the moving boundary, see figure 1(a). The employed block distribution is shown in figure 1(b), where each block has $68 \times 24 \times 24$ cells.

The solid domain is governed by the weak form of the linear momentum balance, and the constitutive law is derived from the hyper-elastic Saint Venant-Kirchhoff material model. The finite element method is used for the spatial discretization of the balance equations and the fully discrete non-linear system is solved with the finite-element solver CalculiX (http://www.calculix.de). The Hilbert-Hugues-Taylor α-method is employed for time discretization, where the parameter α is set to -0.3 and the resulting implicit time stepping is solved using a Newton-Raphson method. The flexible panel is discretized with 196 quadratic hexahedral elements in streamwise direction and two elements along its thickness. The panel is restricted to purely two-dimensional motion (no torsion) so only one element is used across the span. Displacements within the elements are represented with quadratic shape functions. A constant pressure of $1.87p_\infty$ is prescribed in the cavity, where p_∞ is the free-stream static pressure of the flow. This value corresponds to the mean wall-pressure of the flat rigid-wall STBLI over the panel. In order to reduce the computational cost, the adaptive reduced-order model (AROM) of Thari et al. [17] is employed. The method relies on repeated linearizations of the balance equations upon which the number of unknowns is decreased using the mode superposition method [23] with a reduced number of modes (modal truncation augmentation [24] is used to maintain accuracy). For the current simulations, the AROM is build with 10 modes and re-calibrated when the maximum panel displacement exceeds 25% of the panel thickness.

A loosely coupled serial staggered scheme is employed to advance the FSI system in time. The scheme follows the classical Dirichlet-Neumann partitioning, where the fluid inherits displacements from the structure and the structure is loaded by the fluid pressure and viscous stresses.

IV. Results

In this section, we present and compare the corresponding results for the baseline (rigid flat-wall) STBLI and coupled (flexible wall) STBLI simulations, hereafter referred to as baseline and coupled cases. Both simulations were integrated for over 90 flow-through times of the full domain length after the corresponding initial transients. The last instantaneous solution of the baseline case served as initial condition for the coupled simulation, in which the flat panel was allowed to deform. Quantities of interest have been extracted from three-dimensional snapshots, that were recorded at a sampling interval of $0.5\delta_{0,i}/u_\infty$ leading to an ensemble of 8200 snapshots per case.

A. Undisturbed turbulent boundary layer

In order to characterize the approaching TBL, an additional simulation was conducted on the baseline domain without the incident shock. After an initial transient, flow statistics were collected over 12 flow-through times of the full domain length and evaluated at the inviscid impingement point x_{imp}. Table 1 provides a summary of relevant boundary layer parameters at this location.

The corresponding van Driest-transformed mean streamwise velocity profile is included in figure 2(a). It shows excellent agreement with the reference DNS data of Pirozzoli and Bernardini [20] for a Mach 2.0 TBL at a comparable $Re_\tau = 1100$. Density-scaled Reynolds stresses are reported in figure 2(b) and are also in very good agreement with the reference data. Most notably, the magnitude and position of the stress peaks are excellently captured in the present LES.

Inspection of streamwise spectra (not shown here) reveals a dominant inner peak at a wavelength $\lambda_x^+ \approx 700$ and an emerging outer peak at $\lambda_x \approx 6\delta_0$. While this is indicative of incipient scale separation, the largest scales in the TBL are still not expected to meaningfully alter the low-frequency dynamics of the investigated STBLI [3].

Table 1   Relevant boundary layer parameters at the inviscid impingement point x_{imp} without the shock.

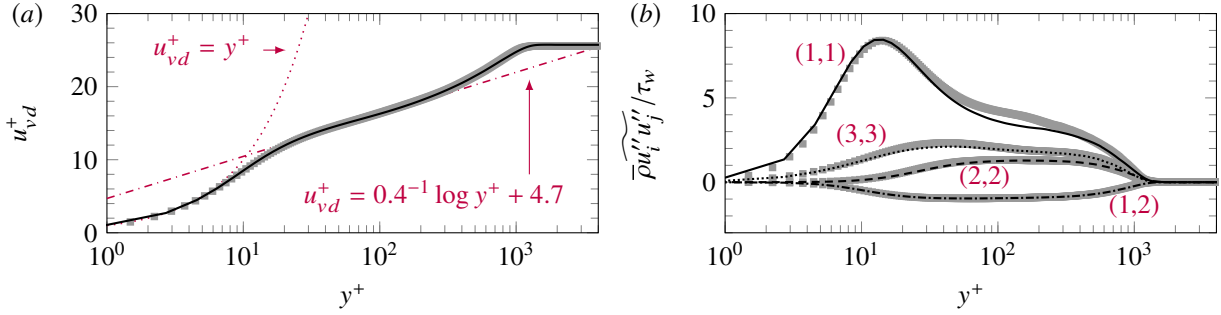| δ_0, mm	θ, mm	H	u_τ, m s^{-1}	$\overline{\rho}_w$, kg m^{-3}	Re_{δ_0}	Re_θ	Re_τ
7.15	0.61	3.19	21.6	0.56	67.1×10^3	5.7×10^3	1226

Fig. 2 (a) Van Driest-transformed mean streamwise velocity profile, and (b) density-scaled Reynolds stresses at the inviscid impingement location without the shock. Legend: (solid lines) present LES, (markers) DNS data of Pirozzoli and Bernardini [20] at $Re_\tau = 1100$. In (b), indices (i, j) distinguish the different Reynolds stresses.
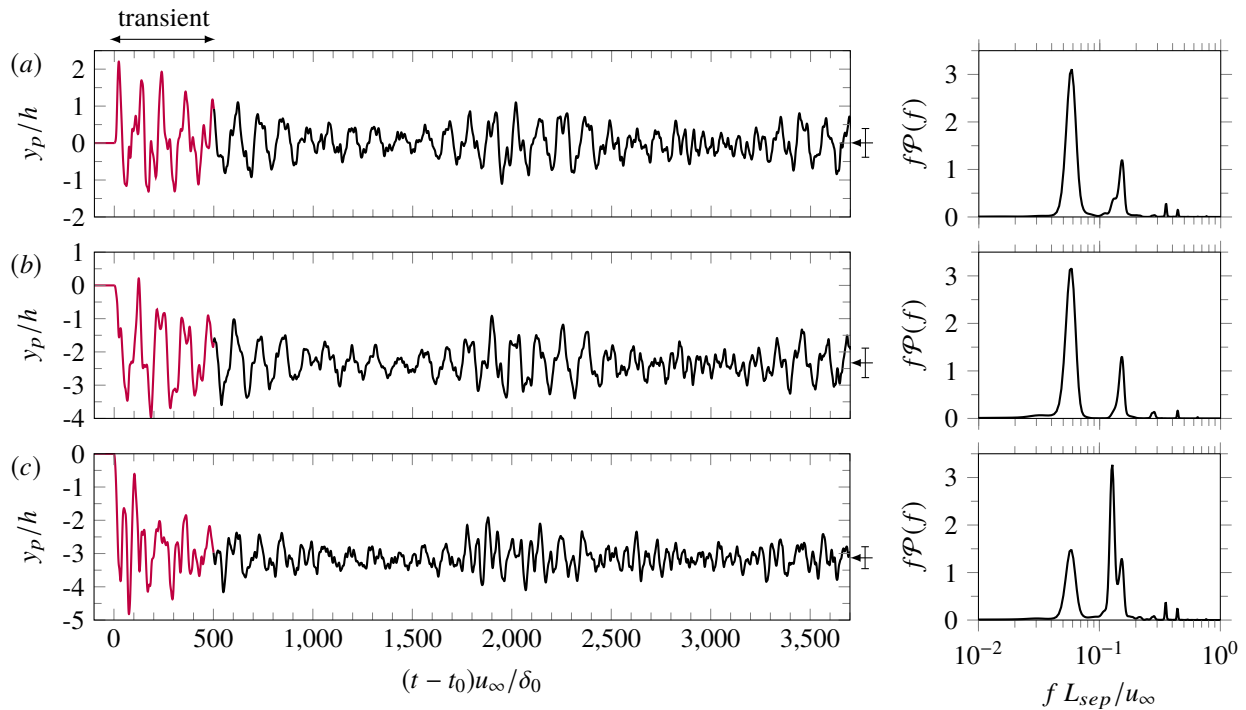

Fig. 3 Instantaneous vertical panel displacements for the (a) quarter point, (b) mid point, and (c) three-quarter point locations along the panel length. Arrows and vertical bars (at the right hand scale) indicate the corresponding mean displacement and its standard deviation. Panels to the right include the power spectral density of the signals.

B. Panel response

The time evolution of vertical panel displacements is shown in figure 3 for the quarter point, mid point and three-quarter point locations along the panel length. The largest displacements are found within the first ~15 flow-through times after the flexible panel is released, which corresponds to the initial transient period required to reach the mean deformation state. This initial transient (indicated in red in figure 3) is excluded from the statistical analysis. For the remaining simulation time, a self-sustained oscillatory behavior with varying oscillation amplitude is observed, which confirms the strong and complex dynamic coupling between the panel and the flow.

Figure 4(a) shows the mean panel deformation together with the envelope of all instantaneous deflection states after the initial transient. The observed mean shape is consistent with the pressure difference, resulting from the pressure distribution caused by the STBLI on top and the constant imposed cavity pressure at the bottom, and has a maximum
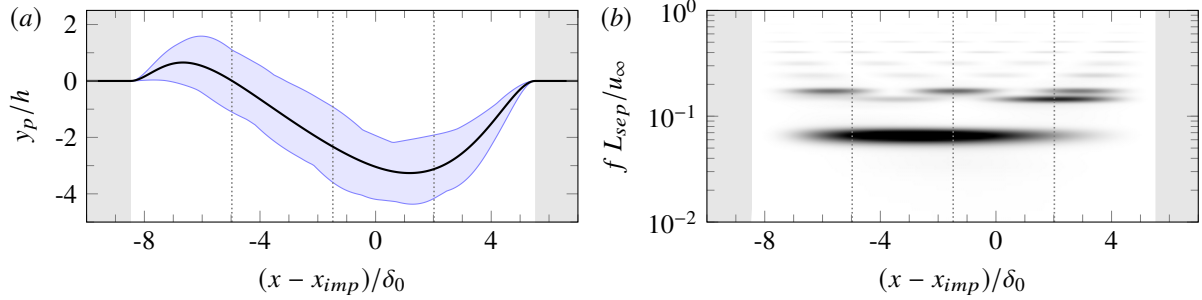
4

Fig. 4 **(a) Mean panel deflection (black) together with the envelope of all instantaneous deflection shapes (blue shade), and (b) pre-multiplied PSD map of displacement signals (increasing linearly from white to black). Vertical dotted lines indicate the quarter point, mid point, and three-quarter point locations along the panel length, and the rigid portion of the wall is shaded in gray**

Table 2   Frequencies of oscillation.

| Natural | | | | Measured | |
| Flat | | Pre-stressed | | | |
Hz	$St_{L_{sep}}$	Hz	$St_{L_{sep}}$	Hz	$St_{L_{sep}}$
134	0.013	538	0.051	593	0.056
375	0.036	1351	0.128	1338	0.127
739	0.070	1554	0.148	1625	0.154

downward deflection that exceeds $3h$ over around 70% of the panel length. The corresponding power spectral density (PSD) map of panel displacements is included in figure 4(b) and provides an indication of the dominant vibration modes and their respective frequencies. PSDs have been estimated using Welch's algorithm, with Hamming windows and 10 segments with 65% overlap (segment length of approximately $650\delta_0/u_\infty$).

As observed in figure 4(b), the first three bending modes account for most of the variance of the displacement signals while higher-order modes contribute only marginally. This is in good agreement with previous studies [12, 14–16]. Interestingly, the first bending mode is not symmetric; rather, its largest contribution is found in the second quarter of the panel, see figure 4(b). The second bending mode is also highly asymmetric and has energetic contributions predominantly in the second half of the panel. Its frequency is very close to that of the third bending mode, which as opposed to the previous two has a rather symmetric effect with respect to the panel half-length.

Note that large static displacements increase the effective stiffness of the panel, thereby requiring higher driving frequencies to resonate. Table 2 reports the first three natural oscillation frequencies for the unloaded flat panel and the pre-stressed deformed panel, which confirm the effective stiffening. These values were obtained with a free-vibration analysis performed with the structural solver, which in the pre-stressed case involved loading with the mean wall-pressure of the coupled simulation. For comparison, table 2 also includes the energetic frequencies identified in the displacement signal of the three-quarter point along the panel length (shown in figure 3(c) with its corresponding PSD). As observed, these frequencies are in close agreement with the natural frequencies of the pre-stressed panel, rather than the flat, which highlights the importance of the mean panel deformation in the dynamic coupling with the flow.

C. Instantaneous and mean-flow organization

Instantaneous impressions of the temperature field are provided in figure 5 for both cases, which illustrate the investigated STBLI topology. Contours of instantaneous (black) and mean (yellow) zero streamwise velocity show the massive flow separation, which is characteristic of strong interactions. Downstream of the separation point, incoming TBL disturbances grow into larger vortical structures as the shear layer moves away from the wall, and they eventually interact with the incident-transmitted shock at the bubble apex. Such shock-vortex interaction and the strong flow deceleration near separation cause visible peaks in the turbulence kinetic energy production [25]. Immediately after the
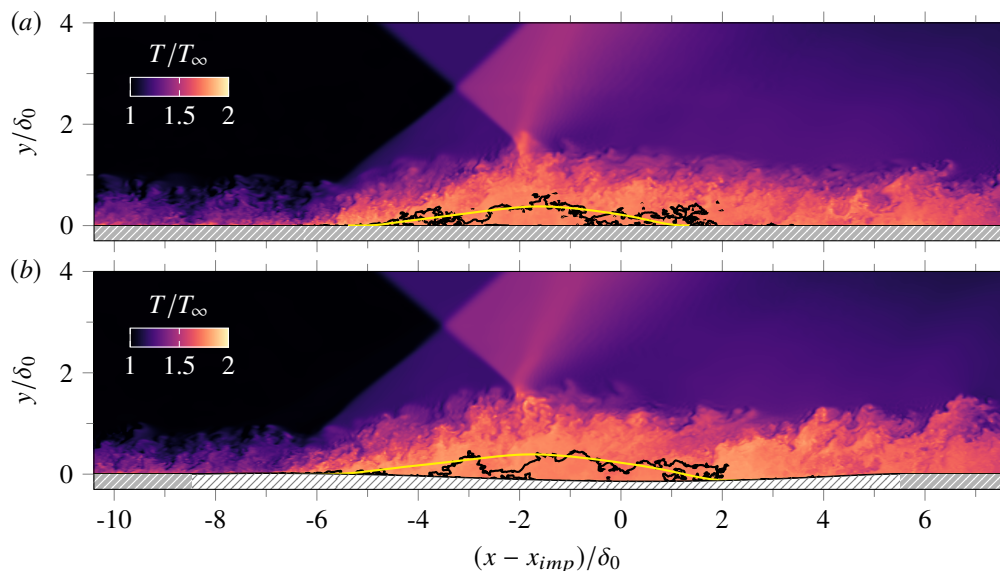
Fig. 5 Instantaneous flow organization: (a) baseline interaction, (b) coupled interaction. Solid lines indicate instantaneous (black) and mean (yellow) iso-contours of zero streamwise velocity, and stripe patterns denote the rigid (gray) and flexible (white) portion of the surface.

bubble apex, the flow is turned towards the wall and the reattachment process is initiated. Both cases exhibit a very mild concave streamline curvature at reattachment, which results in a weak compression fan instead of a coalesced reattachment shock.

Relevant wall-properties are shown in figure 6 to highlight the impact of the moving wall on the interaction. Skin-friction distributions in figure 6(a) show an increase of 15.6% in the streamwise extent of the reverse-flow bubble for the coupled interaction. That is, the separation length L_{sep}, defined as the streamwise distance between mean separation and reattachment points, increases from $6.62\delta_0$ to $7.65\delta_0$ in the presence of the moving panel (the separation point moves $0.42\delta_0$ upstream and the reattachment point moves $0.61\delta_0$ downstream). Furthermore, the initial skin-friction drop and partial recovery at the leading edge of the panel are consistent with the upward mean panel deflection at this location, see figure 4(a). The following decrease in $\langle C_f \rangle$, on the other hand, is attributed to the STBLI and reveals the upstream shift of the separation shock with respect to the baseline, see figure 6(a). This is also apparent in the mean and RMS wall-pressure evolution, which are shown in figures 6(b) and 6(c). Interestingly, the incipient pressure plateau in the separated region also appears more established for the coupled case in figure 6(b), which is generally associated with a stronger interaction [26]. In addition, wall-pressure fluctuations have a 25% higher peak value at the separation-shock foot, see figure 6(c), which evidences the non-negligible impact of dynamic surface displacements on the separation-shock unsteadiness. Larger pressure fluctuations are also found beyond the reattachment location for the coupled interaction, which could be attributed to the presence of stronger vortices in the reattaching shear layer. The probability of reverse-flow is shown in figure 6(d) for both cases, and further confirms the enlargement of the reverse-flow bubble.

D. STBLI dynamics

In order to identify dominant frequencies in the investigated STBLIs, and to assess the corresponding modulation as a result of the panel motion, temporal spectra of wall-pressure, separation-shock location and bubble-volume have been analyzed for both cases.

The pre-multiplied and normalized PSD maps of the wall-pressure are considered first in figures 7(a) and 7(b), the former corresponding to the baseline interaction and the latter to the coupled case. Dashed lines denote the mean separation and reattachment points for each case while the leading and trailing edges of the panel are indicated in figure 7(b) with dotted lines. As observed, the excursion range of the separation shock is located in front of the reverse-flow region in both cases and exhibits a distinct low-frequency signature compared to the incoming TBL. The spectra for the coupled interaction, however, show that the separation-shock motion efficiently conforms to the panel oscillation. The
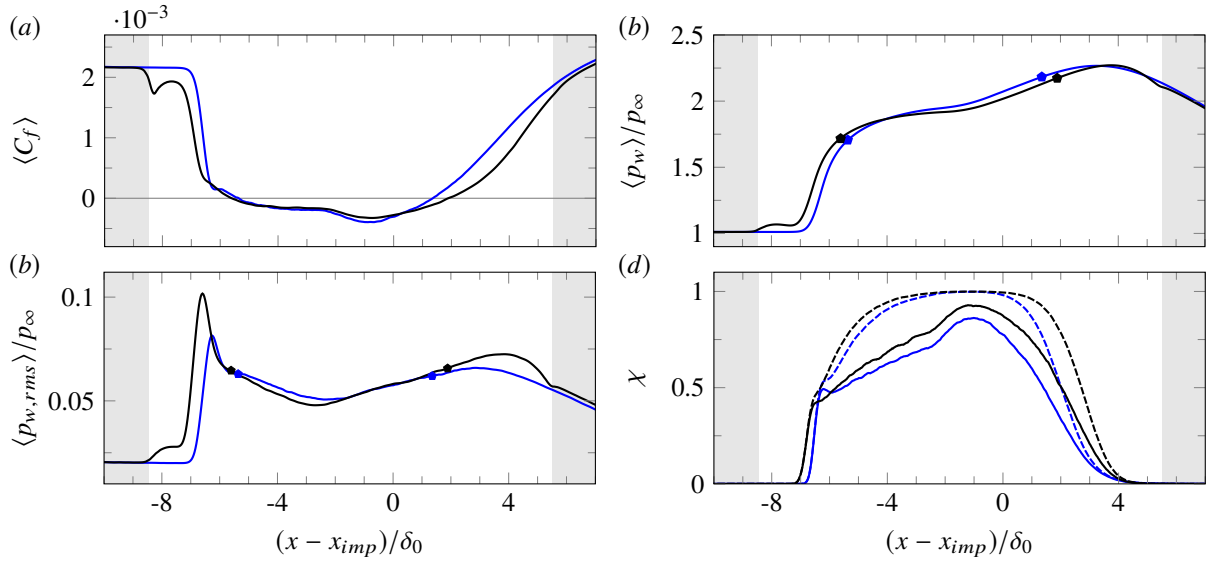
6

Fig. 6   Time- and spanwise-averaged (a) skin-friction, (b) wall-pressure, (c) wall-pressure RMS, and (d) probability of reverse-flow. Line legend: (blue) baseline interaction, (black) coupled interaction. Markers denote the corresponding mean separation and reattachment points, while solid and dashed lines in (d) indicate the reverse-flow probability at the wall and the maximum value along the wall-normal direction, respectively.
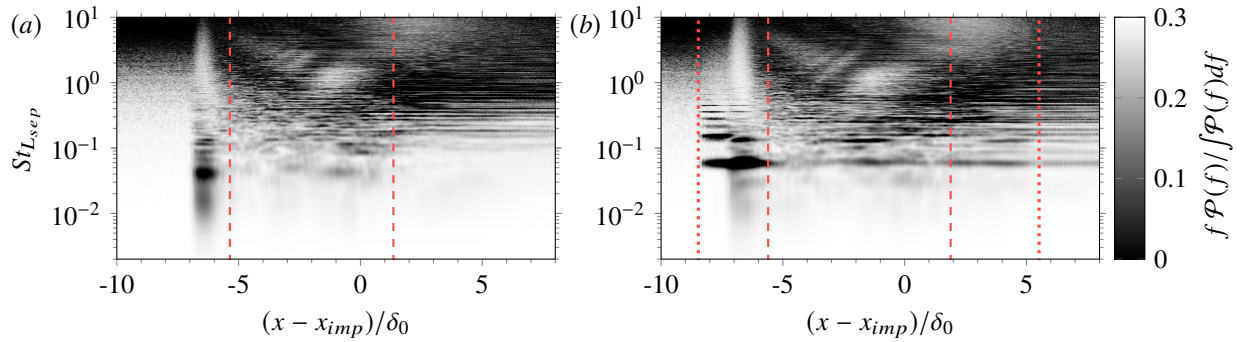

Fig. 7   Pre-multiplied and normalized PSD map of the centerline wall-pressure: (a) baseline interaction, (b) coupled interaction. Dashed lines indicate the mean separation and reattachment locations, and dotted lines in (b) mark the leading and trailing edges of the panel.

most energetic peaks in the low-frequency range for this case correspond to the first and second bending modes of the panel, which are also found energetic upstream of the separation-shock range, throughout the reverse-flow region and beyond reattachment. Energetic content associated with the panel motion, particularly at the first bending frequency, is also visible downstream of the trailing edge of the panel. This suggests that the dynamic fluid-structure coupling results in pressure disturbances that propagate into the downstream flow.

Further insights on the separation-shock dynamics are obtained by inspecting the time evolution of the separation-shock location and its pre-multiplied PSD, which are shown in figure 8(a) for both cases. Instantaneous signals were extracted from the corresponding three-dimensional snapshot sequence, by searching for peak values of the pressure gradient field $|\nabla p|$ in a wall-normal slice outside the boundary layer (at $y = 1.5\delta_0$, before intersecting the incident shock) and then averaging the resulting shock front in span. Note that the shock location in figure 8(a) is referenced with respect to the mean separation-shock location of the baseline case $\langle x_{s,b} \rangle$ for ease of comparison.

Figure 8(a) shows that the separation shock is clearly located more upstream in the presence of the flexible panel. Variations around the mean location are also larger in the coupled case, resulting in a larger standard deviation of the signal (indicated with vertical bars on the right side of the plot). This is in agreement with the increased wall-pressure fluctuation intensity at the separation-shock foot, see figure 6(c). The dominant peak in the corresponding PSD of the separation-shock location signal, shown in the right panel of figure 8(a), confirms that the dynamic coupling between the
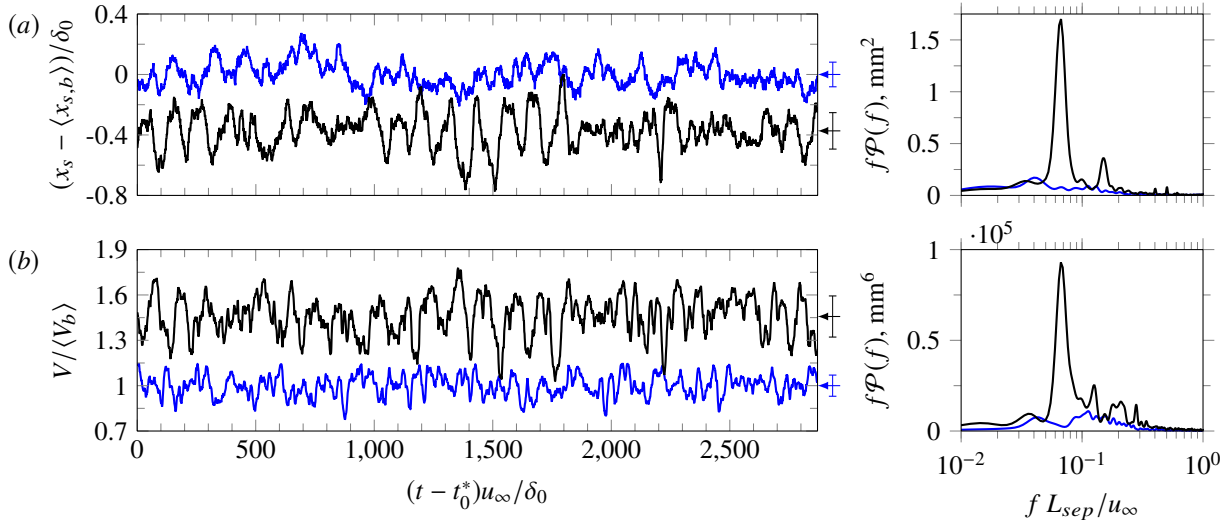
7

Fig. 8 **Time evolution of (a) spanwise-averaged shock position, and (b) separation bubble volume after the transient. Line legend: (blue) baseline interaction, (black) coupled interaction. Arrows and vertical bars indicate the corresponding mean value and its standard deviation, and right panels include the pre-multiplied PSD of the signal.**

separation shock and the moving panel is mainly established through the first bending mode of the panel oscillation (the peak is located precisely at 593 Hz). A secondary and less energetic peak is also visible in the spectra for the coupled case, see figure 8(a), at a frequency $St_{L_{sep}} \approx 0.130$. This is very close to that of the second bending mode of the panel oscillation, which is found at $St_{L_{sep}} \approx 0.127$. Frequencies below the first bending frequency of the panel oscillation are also relatively energetic in the shock-location signal of the coupled interaction, and their level is comparable to the low-frequency content in the baseline case (PSDs are not normalized in this figure). This suggests that the low-frequency dynamics characteristic of flat rigid-wall STBLI coexist with those emerging from the dynamic coupling with the moving panel, rather than being replaced by them.

The time evolution of the reverse-flow bubble volume is shown in figure 8(b), and the observed changes in the presence of the moving panel are in close qualitative agreement with those discussed for the separation-shock location. Note that volume signals in figure 8(b) have been normalized with the mean bubble volume for the baseline case $\langle V_b \rangle$. On average, the bubble volume increases by 50% in the presence of the flexible panel (if only the fluid domain above $y = 0$ is considered, the increase is 15%). From the corresponding PSD, it is also clear that the dominant frequency in the bubble-volume signal is associated with the first bending mode of panel oscillation. Higher frequencies appear also energetic, but a direct connection with a dominant frequency of the panel motion cannot be established.

E. Modal analysis

In order to relate global flow phenomena to the energetic bending frequencies of the panel, we perform dynamic mode decomposition (DMD, [27]) of the LES data for each case. A total of $N_s = 8200$ snapshots sampled at a frequency $f_s = 2u_\infty/\delta_{0,i}$ are used (per case) to produce a modal decomposition with high statistical significance. The considered snapshots include the instantaneous three-dimensional streamwise velocity and pressure fields. For the coupled interaction, the corresponding panel displacements are also appended to the instantaneous snapshot data so that a statistical link between flow dynamics and panel motion can be directly established.

In addition to the standard DMD, further dimensionality reduction is sought via the sparsity-promoting version of the DMD algorithm (SPDMD, [28]). This algorithm facilitates mode selection from the DMD solution by detecting modal flow features that have the strongest influence on the entire snapshot history. For the coupled interaction, the LES results have so far shown that the STBLI flow strongly resonates with the first bending mode of the panel oscillation. This emerging narrow-banded behavior in an otherwise broadband spectrum makes the investigated FSI particularly suitable for the dimensionality reduction granted by the SPDMD algorithm [28].

The corresponding modal amplitudes and frequencies resulting from standard DMD (circles) and SPDMD (crosses) of the considered fields are displayed in figures 9(a) and 9(b) for the baseline and coupled interactions, respectively. The
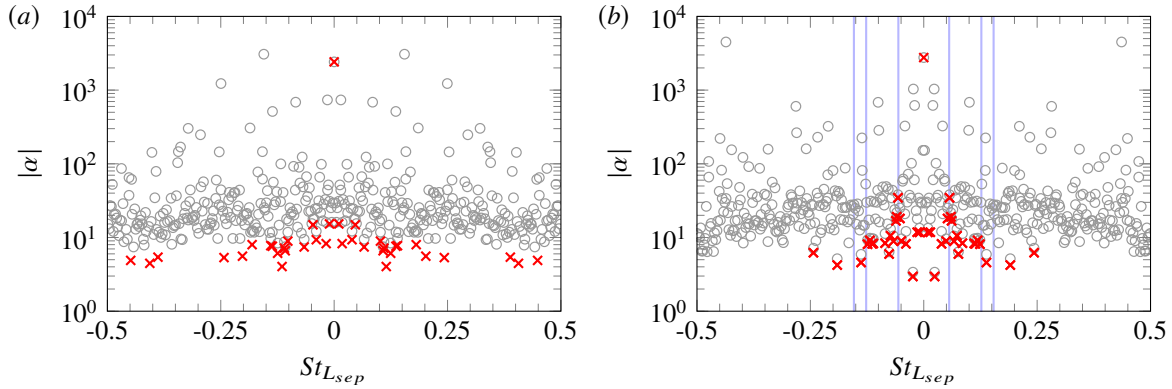
8

Fig. 9 **Modal amplitude distribution: (a) baseline interaction, (b) coupled interaction. Symbol legend: (circles) DMD solution, (crosses) SPDMD solution. In (b), solid blue lines indicate the first three bending frequencies of the panel as measured from the PSD of panel displacements.**

regularization parameter in the SPDMD algorithm has been set such that the number of retained DMD modes, hereafter also referred to as SPDMD modes, is 41 for each case. In this way, the resulting sparse solution is composed of a strong mean mode and 20 complex conjugate pairs, see figures 9(a) and 9(b). The maximum modal frequency in each DMD solution is $St_{L_{sep}} = 9.5$; however, figures only show $St_{L_{sep}} \leq 0.5$ to focus on the SPDMD modes, which concentrate at low-frequencies. Their amplitudes are also different from the corresponding amplitudes of the original DMD modes since the sparsity-promoting algorithm recomputes them for an optimal representation of the entire data sequence with the retained sparse structure [28].

The SPDMD solution for the baseline interaction is spread over the range of frequencies shown in figure 9(a). While the largest amplitudes are still found at the lower end of the spectrum, that is, below $St_{L_{sep}} = 0.1$, the retained dynamics do not appear to be tonal. This is consistent with the low-frequency unsteadiness of STBLI being broadband. The SPDMD solution for the coupled interaction, in turn, presents a distinct tone precisely at the first bending frequency of the panel oscillation, see figure 9(b). The dominant frequencies measured in the spectra of panel displacements are also indicated in the figure (solid lines), and the one associated with the first bending mode essentially intersects the largest modal amplitude with non-zero frequency. This confirms the excellent capabilities of the SPDMD method in detecting and isolating the main system dynamics.

In addition to the distinct tone, the sparse modal representation of the coupled interaction also includes dynamic modes below the first bending frequency of the panel oscillation, and their modal amplitudes are comparable to those for the baseline interaction in the same frequency range, see figure 9(a). The second bending mode is also present in the SPDMD solution of figure 9(b), but it does not emerge as a distinct peak in modal amplitude, unlike the first bending mode. The third bending mode, on the other hand, cannot be directly associated with a particular SPDMD mode, indicating that the STBLI flow does not resonate at this frequency.

Figure 10 depicts the real part of a representative low-frequency mode in the SPDMD solution of the coupled interaction. The corresponding modal frequency is $St_{L_{sep}} = 0.015$, which is lower than the first bending frequency of the panel oscillation (found at $St_{L_{sep}} = 0.056$). The modal pressure in the left panel of figure 10 highlights the expected connection between the low-frequency unsteadiness of STBLI and longitudinal excursions of the separation shock. In addition, these excursions appear associated with pressure fluctuations of opposite sign near reattachment, which is consistent with expansions and contractions of the reverse-flow bubble from both ends. The modal streamwise velocity field in the center panel of figure 10 additionally reveals a statistical link between the low-frequency unsteadiness of the separation shock and alternating velocity streaks that originate near the separation point. Similar streaks were also identified by Priebe et al. [29] in a Mach 2.9 compression ramp flow via modal analysis. In agreement with their results, we find that these velocity structures meander in the spanwise direction. The strongest velocity fluctuations are found at the leading edge of the bubble and in the downstream flow, whereas the streak strength is highly damped at the bubble apex due to the interaction with the incident-transmitted shock. This differs from the compression ramp flow case of Priebe et al. [29] where an incident shock is absent. The modal displacement field of the considered low-frequency mode, see the right panel of figure 10, shows that the panel passively adapts to the oscillating flow.
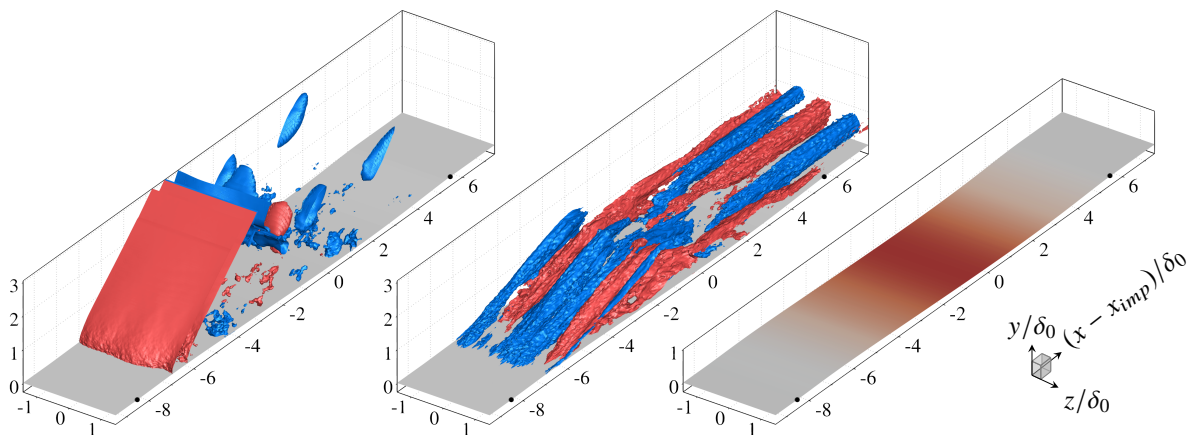
9

Fig. 10 Real part of a representative low-frequency mode in the SPDMD solution of the coupled interaction ($St_{L_{sep}} = 0.015$): (left) modal pressure, (center) modal streamwise velocity, (right) modal displacements. Front and rear edges of the flexible panel are indicated with black circles. Iso-contours in the left and center panels indicate strong positive (red) and negative (blue) fluctuations, and the corresponding surface geometry is indicated in gray. In the right panel, the surface geometry is colored by the modal displacements.

While not shown here, it is important to note that low-frequency modes for the baseline interaction appear qualitatively very similar to the mode depicted in figure 10. Combined with the fact that the corresponding modal amplitudes below the first bending frequency of the panel oscillation are also very similar in both cases, the SPDMD analysis thus confirms that the emerging FSI dynamics in the coupled interaction coexist with, rather than replace, the characteristic low-frequency (non-FSI) dynamics of STBLI.

Attention is now turned towards the dynamic mode associated with the first bending frequency of the panel oscillation, at $St_{L_{sep}} = 0.056$. Its real part is shown in figure 11. This mode differs from the low-frequency mode shown in figure 10; most notably, fluctuation fields associated with flow variables exhibit a clear spanwise coherence that is consistent with the two-dimensional bending motion of the panel. This is particularly evident in the modal streamwise velocity field, see the center panel of figure 11, where spanwise-coherent fluctuations of the entire shear layer are visible instead of alternating streaks. The modal pressure, see the left panel of figure 11, shows quasi-two-dimensional fluctuations of opposite sign at separation and reattachment and strong fluctuations propagating into the downstream flow. This observation is in agreement with the wall-pressure spectra of figure 7(b) where energetic content at the first bending frequency is visible beyond the trailing edge of the panel.

In order to better understand the dynamic coupling at the first bending frequency of the panel oscillation, figures 12(a) shows the evolution of the mid point displacement of the panel, the separation-shock location, and the reverse-flow bubble volume over two periods of oscillation (the modal shape of figure 11 corresponds to phase θ_1 indicated at the top). Expansions and contractions of the reverse-flow bubble (dotted line) closely follow the panel motion (solid red line), with downward panel bending promoting bubble growth. This behavior is consistent with the mean-flow analysis of section IV.C, which also shows an enlarged reverse-flow bubble as a result of the mostly downward mean panel deflection. The separation-shock location signal, indicated with a dashed line in figure 12(a), clearly follows the resulting bubble variations with a phase shift of approximately 1.2π. Interestingly, the measured time lag between both signals (bubble volume and shock location) is precisely the acoustic propagation time from reattachment to the separation-shock foot, which supports the hypothesis of a downstream instability being the main driver of the separation-shock unsteadiness [3].

Further insight into the dynamic coupling can be gained by inspecting the corresponding variation of the integral panel load, which is indicated with a solid black line in figure 12(b). The fraction of the load on the first and second half of the panel, which make up the integral panel load, are also indicated in the figure as dashed and dotted lines, respectively. By first comparing figures 12(a) and 12(b), it is clear that the separation-shock motion strongly impacts the load on the first half, while the trailing edge of the bubble, which is associated with the reattachment compression, influences the load on the second half. The particular evolution of these signals, as well as their relative offset, leads to
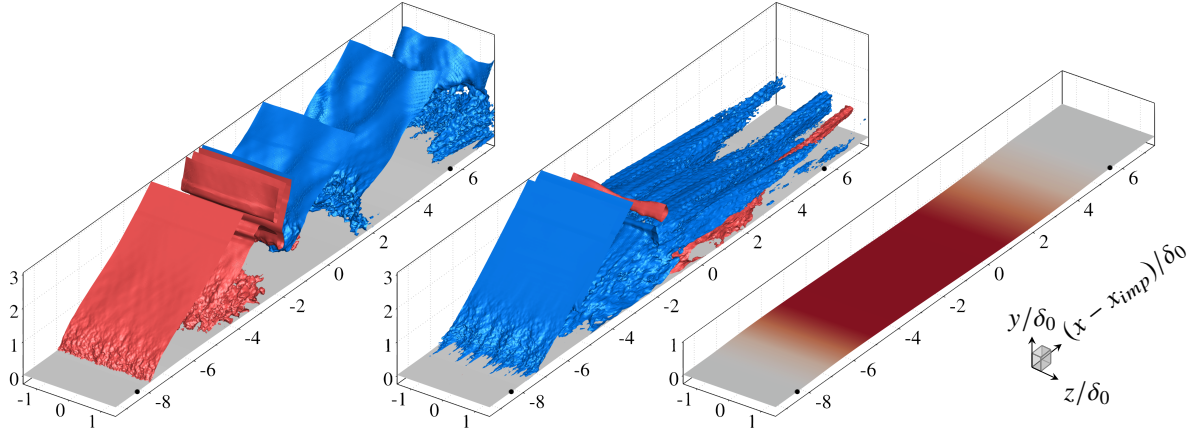
10

Fig. 11 Real part of the SPDMD mode associated with the first bending mode of panel oscillation in the coupled interaction ($St_{L_{sep}}$ = 0.056): (left) modal pressure, (center) modal streamwise velocity, (right) modal displacements. For additional details, see figure 10.
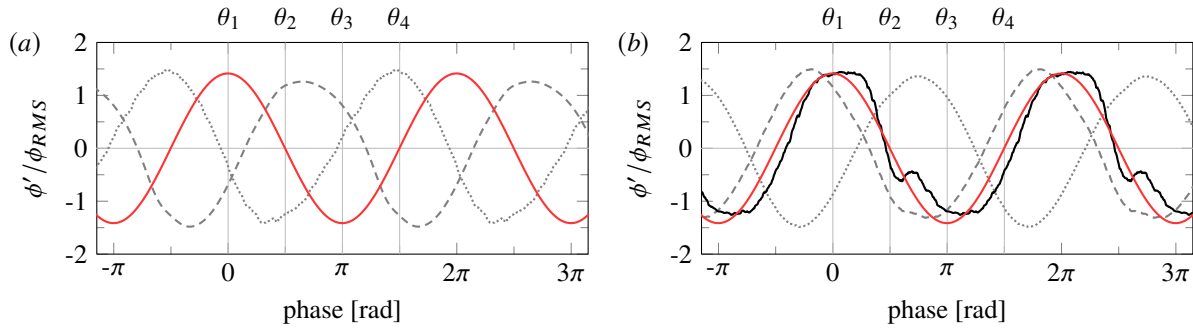

Fig. 12 Variation of different quantities of interest for the pure oscillation based on the spanwise-averaged dynamic mode of figure 11. Line legend in (a): (solid red) mid point displacement of the panel (also included in (b)), (dashed) separation-shock location, (dotted) reverse-flow bubble volume. Line legend in (b): (solid black) integrated load over the whole panel, (dashed) integrated load over the first half of the panel, (dotted) integrated load over the second half of the panel. For reference, four equispaced phases within one cycle are indicated at the top of each panel.

an integral panel load that essentially increases during the upward bending and decreases during the downward bending, see figure 12(b), in which the mid point panel displacement signal is also included as a solid red line for reference.

Before concluding, we note that the dynamic mode associated with the second bending frequency of the panel oscillation is similar to the low-frequency mode of figure 10, but with a slightly narrower excursion domain of the separation shock and moderate spanwise shock wrinkling. The analogous SPDMD modes for the baseline interaction are also qualitatively similar to this second bending mode, which suggests that the STBLI flow is not strongly modulated at this frequency. In agreement with the observations made in the previous section, the present modal analysis thus shows that the FSI coupling is primarily established through the first bending mode of panel oscillation.

V. Conclusions

Numerical simulations have been performed to investigate the fluid-structure interaction (FSI) between a Mach 2.0 shock-wave/turbulent boundary-layer interaction (STBLI) and a flexible panel. A partitioned FSI approach comprising a finite-volume fluid solver and a finite-element structural solver is employed for the calculations, together with the adaptive reduced-order model of Thari et al. [17] to achieve long integration times. Results are compared against the

11

baseline configuration, a flat rigid-wall STBLI at the same flow conditions.

The panel exhibits self-sustained oscillatory behavior with varying oscillation amplitude, confirming the strong and complex dynamic coupling with the flow over a broad frequency range. The first three bending modes of the panel oscillation are found to make up most of the unsteady panel response, which is in agreement with previous studies. The observed modal frequencies are in close agreement with natural oscillation frequencies of the pre-stressed panel, which differ significantly from those for the flat configuration. This highlights the importance of the mean panel deformation and the corresponding stiffening in the system dynamics. Furthermore, an enlarged reverse-flow region is found in the presence of the moving panel, with the separation shock being located further upstream compared to the baseline interaction. Higher wall-pressure fluctuation intensities are also measured at the separation-shock foot and beyond the reattachment point, and spectral analysis of wall-pressure, separation-shock location and bubble-volume variations indicates that the STBLI flow resonates with the panel oscillation, primarily at the first bending frequency. This is further confirmed by sparsity-promoting dynamic mode decomposition [28] of the flow and displacement data, which identifies this frequency as the most dominant and successfully isolates the associated FSI dynamics. The corresponding modes reveal variations in the reverse-flow region that follow the panel bending motion (with downward bending promoting bubble growth) and precede the separation-shock motion. At the same time, the response of the STBLI flow significantly alters the panel load in a restoring fashion, which sustains the dynamic fluid-structure coupling. Dynamic modes that are not associated with the first bending frequency of the panel oscillation, in turn, are very similar to those obtained for the baseline interaction. This indicates that the STBLI dynamics emerging from the unsteady FSI coexist with, rather than replace, the characteristic low-frequency (non-FSI) content of the interaction.

Based on present results, it is clear that dynamic FSI involving STBLI and flexible panels can accentuate the undesirable features of STBLI and potentially jeopardize structural integrity. Even though results may vary depending on impingement location, interaction strength or cavity pressure, the use of flexible structural components as passive flow control devices (as hypothesized in literature) is not supported by the present findings.

References

[1] Dupont, P., Haddad, C., and Debieve, J. F., "Space and time organization in a shock-induced separated boundary layer," *Journal of Fluid Mechanics*, Vol. 559, 2006, pp. 255–277.

[2] Délery, J., and Dussauge, J.-P., "Some physical aspects of shock wave/boundary layer interactions," *Shock Waves*, Vol. 19, No. 6, 2009, p. 453.

[3] Clemens, N. T., and Narayanaswamy, V., "Low-frequency unsteadiness of shock wave/turbulent boundary layer interactions," *Annual Review of Fluid Mechanics*, Vol. 46, 2014, pp. 469–492.

[4] Gogulapati, A., Deshmukh, R., Crowell, A. R., McNamara, J. J., Vyas, V., Wang, X. Q., Mignolet, M., Beberniss, T., Spottswood, S. M., and Eason, T. G., "Response of a panel to shock impingement: modeling and comparison with experiments," *55th AIAA/ASMe/ASCE/AHS/SC Structures, Structural Dynamics, and Materials Conference-SciTech Forum and Exposition 2014*, 2014.

[5] Blevins, R. D., Holehouse, I., and Wentz, K. R., "Thermoacoustic loads and fatigue of hypersonic vehicle skin panels," *Journal of Aircraft*, Vol. 30, No. 6, 1993, pp. 971–978.

[6] Whalen, T. J., Schöneich, A. G., Laurence, S. J., Sullivan, B. T., Bodony, D. J., Freydin, M., Dowell, E. H., and Buck, G. M., "Hypersonic fluid–structure interactions in compression corner shock-wave/boundary-layer interaction," *AIAA journal*, 2020.

[7] Eason, T. G., and Spottswood, S., "A structures perspective on the challenges associated with analyzing a reusable hypersonic platform," *54th AIAA/ASME/ASCE/AHS/ASC Structures, Structural Dynamics, and Materials Conference*, 2013, p. 1747.

[8] Dolling, D. S., "Fifty years of shock-wave/boundary-layer interaction research: what next?" *AIAA Journal*, Vol. 39, No. 8, 2001, pp. 1517–1531.

[9] Gaitonde, D. V., "Progress in shock wave/boundary layer interactions," *Progress in Aerospace Sciences*, Vol. 72, 2015, pp. 80–99.

[10] McNamara, J. J., and Friedmann, P. P., "Aeroelastic and aerothermoelastic analysis in hypersonic flow: past, present, and future," *AIAA Journal*, Vol. 49, No. 6, 2011, pp. 1089–1122.

[11] Willems, S., Gülhan, A., and Esser, B., "Shock induced fluid-structure interaction on a flexible wall in supersonic turbulent flow," *Progress in Flight Physics*, Vol. 5, 2013, pp. 285–308.

[12] Musta, M. N., Ahn, Y.-J., Eitner, M. A., Sirohi, J., and Clemens, N., "Unsteadiness in Shock/Boundary-Layer Interaction Over a Compliant Panel at Mach 2," *AIAA Paper*, 2022-4136, 2022.

[13] Eitner, M. A., Ahn, Y.-J., Musta, M. N., Sirohi, J., and Clemens, N., "Effect of Ramp-Induced Shock/Boundary Layer Interaction on the Vibration of a Compliant Panel at Mach 5," *AIAA Paper*, 2023-0081, 2023.

[14] Spottswood, S., Eason, T., and Beberniss, T., "Influence of shock-boundary layer interactions on the dynamic response of a flexible panel," *Proceedings of the International Conference on Noise and Vibration Engineering ISMA*, Vol. 2012, 2012, pp. 603–616.

[15] Shinde, V., McNamara, J., and Gaitonde, D., "Dynamic interaction between shock wave turbulent boundary layer and flexible panel," *Journal of Fluids and Structures*, Vol. 113, 2022, p. 103660.

[16] D'Aguanno, A., Quesada Allerhand, P., Schrijer, F. F. J., and van Oudheusden, B. W., "Characterization of shock-induced panel flutter with simultaneous use of DIC and PIV," *Experiments in Fluids*, Vol. 64, No. 1, 2023, p. 15.

[17] Thari, A., Pasquariello, V., Aage, N., and Hickel, S., "Adaptive reduced-order modeling for non-linear fluid–structure interaction," *Computers & Fluids*, Vol. 229, 2021, p. 105099.

[18] Hickel, S., Egerer, C. P., and Larsson, J., "Subgrid-scale modeling for implicit large eddy simulation of compressible flows and shock-turbulence interaction," *Physics of Fluids*, Vol. 26, No. 10, 2014, p. 106101.

[19] Xie, Z.-T., and Castro, I. P., "Efficient generation of inflow conditions for large eddy simulation of street-scale flows," *Flow, Turbulence and Combustion*, Vol. 81, No. 3, 2008, pp. 449–470.

[20] Pirozzoli, S., and Bernardini, M., "Turbulence in supersonic boundary layers at moderate Reynolds number," *Journal of Fluid Mechanics*, Vol. 688, 2011, pp. 120–168.

[21] Laguarda, L., and Hickel, S., "Analysis of improved digital filter inflow generation methods for compressible turbulent boundary layers," *Computers & Fluids (under review)*, 2023.

[22] Pasquariello, V., Hammerl, G., Örley, F., Hickel, S., Danowski, C., Popp, A., Wall, W. A., and Adams, N. A., "A cut-cell finite volume–finite element coupling approach for fluid–structure interaction in compressible flow," *Journal of Computational Physics*, Vol. 307, 2016, pp. 670–695.

[23] Dowell, E. H., and Hall, K. C., "Modeling of fluid-structure interaction," *Annual Review of Fluid Mechanics*, Vol. 33, 2001, p. 445.

[24] Dickens, J., Nakagawa, J., and Wittbrodt, M., "A critique of mode acceleration and modal truncation augmentation methods for modal response analysis," *Computers & structures*, Vol. 62, No. 6, 1997, pp. 985–998.

[25] Pasquariello, V., Grilli, M., Hickel, S., and Adams, N. A., "Large-eddy simulation of passive shock-wave/boundary-layer interaction control," *International Journal of Heat and Fluid Flow*, Vol. 49, 2014, pp. 116–127.

[26] Délery, J., Marvin, J. G., and Reshotko, E., "Shock-wave boundary layer interactions," AGARD-AG *Tech. Rep.* 280, 1986.

[27] Schmid, P. J., "Dynamic mode decomposition of numerical and experimental data," *Journal of Fluid Mechanics*, Vol. 656, 2010, pp. 5–28.

[28] Jovanović, M. R., Schmid, P. J., and Nichols, J. W., "Sparsity-promoting dynamic mode decomposition," *Physics of Fluids*, Vol. 26, No. 2, 2014, p. 024103.

[29] Priebe, S., Tu, J. H., Rowley, C. W., and Martín, M. P., "Low-frequency dynamics in a shock-induced separated flow," *Journal of Fluid Mechanics*, Vol. 807, 2016, pp. 441–477.